

Laser Treatment of HVOF Coating: Modeling and Measurement of Residual Stress in Coating

A.F.M. Arif and B.S. Yilbas

(Submitted June 17, 2007; in revised form November 30, 2007)

High-velocity oxy-fuel (HVOF) coating of diamalloy 1005 (similar to Inconel 625 alloy) onto the Ti-6Al-4V alloy is considered and laser-controlled melting of the coating is examined. The residual stress developed after the laser treatment process is modeled using the finite element method (FEM). The experiment is conducted to melt the coating using a laser beam. The residual stress measurement in the coating after the laser treatment process is realized using the XRD technique. The morphological and metallurgical changes in the coating are examined using scanning electron microscopy (SEM) and energy dispersive spectroscopy (EDS). It is found that the residual stress reduces at the coating-base material interface and the residual stress predicted agrees with the XRD measurements. A compact and crack-free coating is resulted after the laser treatment process.

Keywords coating, HVOF, laser, melting, residual, stress

1. Introduction

High-velocity oxy-fuel (HVOF) coating finds application in industry, in particular power industry, to protect surfaces from high temperature and harsh environments. However, the coating involved is thermal spraying and mechanical anchoring of the splats at the base material surface. The inhomogeneous structure in the coating is resulted due to the semi-molten state and oxidation of some splats during the coating process. In this case, some of the splats remain as round solid structure in the coating. The thermal integration in the coating through control melting provides coating homogeneity and improves bonding strength at the coating-base material interface. The laser heating process is one of the alternatives for the thermal integration of the HVOF coating through control melting. However, the stress levels in the coating upon solidification become important. Consequently, investigation into the laser heating of HVOF coating and the stress levels in the coating after the laser treatment process becomes essential.

Considerable research studies were carried out to examine the laser heating of HVOF coating. The laser melting of HVOF coating was examined by Tuominen et al. (Ref 1). They indicated that the laser re-melting resulted in homogenization of the coating structure. The electron beam re-melting of HVOF coating was studied by Hamatani and Miyazaki (Ref 2). They showed that low melting speed and homogeneous heating reduced the unevenness of the surface of the number of pores in the coating. The laser surface treatment of HVOF coating was carried out by Oksa et al. (Ref 3). They successfully sealed the

coating surface for corrosion prevention. HVOF coating and the laser treatment were investigated by Suutala et al. (Ref 4). They observed that the cracks occurred in the coating after the laser treatment and the crack orientation was perpendicular to the laser processing direction. Adhesion testing of coatings produced via arc spray, HVOF, and laser cladding was carried out by Hjornhede and Nylund (Ref 5). They indicated that the coatings deposited with the laser technique did not show de-lamination. The effect of laser glazing on the microstructure of the HVOF coating was examined by Kumari et al. (Ref 6). They showed that laser glazing of coatings affected the surface roughness in either way depending on the coating composition as well on the treatment parameters. Laser-produced functionally graded coatings were examined by Riabkina-Fishman et al. (Ref 7). They showed that the laser treatment resulted in the coating, which had wear resistance five times higher than that of untreated coatings. High-power laser treatment of HVOF coating was considered by Tuominen et al. (Ref 8). They showed that the laser treatment improved significantly the coatings homogeneity. HVOF coating and the laser treatment of the coated surface was investigated by Yilbas et al. (Ref 9). They carried out three-point bending tests to assess the mechanical response of the coating. However, the model study for the residual stress developed after the laser treatment was omitted. Consequently, further investigation into the laser melting of HVOF coating including the modeling of the residual stress development after the laser treatment process becomes essential.

In the present study, the laser melting of HVOF coating sprayed onto Ti-6Al-4V alloy is considered and the residual stress levels in the coating and coating-base material interface are predicted using the finite element method (FEM). An experiment is carried out to melt the coating using a laser beam. The data used in the simulation resemble the experimental conditions. The residual stress developed in the coating after the laser treatment process is measured using the XRD technique. SEM and EDS are carried out to examine the morphological and the metallurgical changes in the coating prior and after the laser treatment process.

A.F.M. Arif and B.S. Yilbas, Mechanical Engineering Department, KFUPM, Box 1913, Dhahran 31261, Saudi Arabia. Contact e-mail: bsyilbas@kfupm.edu.sa.

2. Mathematical Analysis

The transient diffusion equation based on the Fourier heating model can be written in the three-dimensional Cartesian coordinates as:

$$\rho C_p \frac{\partial T}{\partial t} = k \left(\frac{\partial^2 T}{\partial x^2} + \frac{\partial^2 T}{\partial y^2} + \frac{\partial^2 T}{\partial z^2} \right) + u \rho C_p \frac{\partial T}{\partial y} + S_0 \quad (\text{Eq 1})$$

where x , y , and z are the axes (Fig. 1), u is the scanning speed of the laser beam, ρ is the density, C_p is the specific heat capacity, and k is the thermal conductivity. It should be noted that the laser heating situation is considered to be a constant temperature heat source at the workpiece surface $S_0 = I_0(1 - r_f)(e^{-(x^2+z^2)/a^2})$ with a radius a (laser beam radius at focused surface) in the x - y plane, I_0 is the peak power intensity, r_f is the surface reflectivity, and a depth of melt layer is limited with the thickness of the coating along the y -axis. These conditions represent the situation such that the coating temperature does not reach the evaporation temperature of the substrate material along the z -axis in the x - y plane where laser beam is located (Fig. 1). At the free surface (in x - y plane at $z = 0$), a convective boundary is assumed, therefore, the corresponding boundary condition is:

$$\text{At } z = 0 \text{ (at the surface)} \rightarrow \frac{\partial T}{\partial y} = \frac{h}{k}(T_s - T_o)$$

where h is the heat transfer coefficient and T_s and T_o are the surface and reference temperatures, respectively. In addition, at a distance far away from the surface in the x - y plane, temperature becomes the same as the reference temperature. This yields the boundary condition of:

$$\text{At } x \text{ and } y = \infty \rightarrow T = T_\infty \quad (T_o, \text{ Specified})$$

Initially, the substrate material is assumed to be at a reference temperature (T_o), therefore, the initial condition becomes:

$$\text{At } t = 0 \rightarrow T = T_\infty \quad (T_o, \text{ Specified})$$

To solve Eq. 1 an explicit scheme is employed. The details of the numerical scheme are given in Ref. 10. The stability criteria due to time increment are considered for a stable solution; therefore, the time increment is limited by:

$$\left(\frac{2k}{\rho C_p \Delta x^2} + \frac{2k}{\rho C_p \Delta y^2} + \frac{2k}{\rho C_p \Delta z^2} \right) \Delta t \leq 1$$

The calculation domain is divided in to grids and grid independence test is being performed for different grid size and orientation. The material properties and simulation conditions for Eq. 1 are given in Table 1(a) and (b).

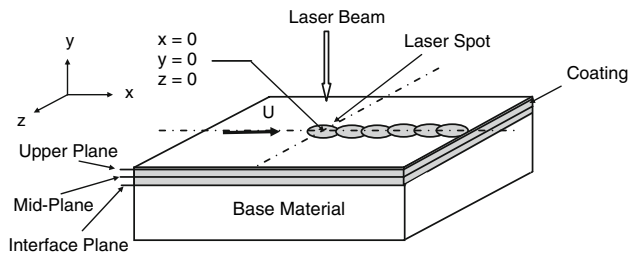


Fig. 1 Cross section of the laser heating situation and coordinate system

2.1 Finite Element Modeling

Finite element method is one of the most accepted and widely used tool for the solution of nonlinear partial differential equations which arises during the mathematical modeling of various processes. The modeling of laser heating, involving phase change of substrate material, is a highly nonlinear-coupled thermo-mechanical phenomenon. The modeling of such a process is very involved as various physical phenomena are interacting, e.g., heat flow, complicated molten metal dynamics, microstructure evolution, and overall thermo-

Table 1 (a) Mechanical and thermal properties of Ti-6Al-4V alloy used in the simulations. (b) Mechanical and thermal properties of Inconel 625 alloy used in the simulations

(a)										
Temp., K	373	478	588	698	813	923				
$\alpha \times 10^{-6}$, 1/K	8.6	9.0	9.2	9.4	9.5	9.7				
ν	0.342									
E , GPa	113.6									
ρ , kg/m ³	4430									
Temp., K	373	473	673	873	1073	1273	1473	1773		
K , W/mK	30.5	24.5	20.4	19.4	19.7	20.7	22.0	24.5		
C_p , J/kgK	300	465	551	591	633	675	620	686		
(b)										
Temp., K	303	366	477	589	700	1273	1473	1673	1873	2073
E , GPa	208	201	199	191	184	176	168	157	146	129
Temp., K	447	589	700	811	922	1033	1144	1255		
$\alpha \times 10^{-6}$, 1/K	13.1	13.5	13.9	14.4	15.1	15.7	16.6	17.3		
ν	0.36									
ρ , kg/m ³	8440									
Temp., K	300	373	473	573	673	773	873			
K , W/mK	9.8	11.4	13.4	15.5	17.6	19.6	21.3			
C_p , J/kgK	429	446	463	480	496	513	560			

mechanical response of the structure. It is indeed very cumbersome to account for all the couplings that exist. In computational mechanics, high degree of simplification is used and most of these couplings are ignored based on their weak nature. The moving heat source results in localized heat generation and large thermal gradients. The nonuniform temperature distribution results in thermal stresses and distortions. The basic theory describing the behavior of continuum combines the theory of heat transfer through conduction and convection and elasto-plasticity. To analyze the phase change problem, a nonlinear transient thermal analysis is performed by employing enthalpy method. To account for latent heat evolution during phase change, the enthalpy of the material as a function of temperature is incorporated in the energy equation.

For structural response, the finite element formulation is based on the principle of virtual work. From PVW, a virtual (very small) change of the internal strain energy (δU) must be offset by an identical change in external work due to the applied loads (δV). Considering the strain energy due to thermal stresses resulting from the constrained motion of a body during a temperature change, PVW yields:

$$\{\delta u\}^T \int_{\text{vol}} [B]^T [D] [B] dv \{u\} = \{\delta u\}^T \int_{\text{vol}} [B]^T [D] \{\epsilon^{\text{th}}\} dv$$

Noting that the $\{\delta u\}^T$ vector is a set of arbitrary virtual displacements common in all of the above terms, the condition required to satisfy above equation reduces to:

$$[K]\{u\} = \{F^{\text{th}}\}$$

where

$$[K] = \int_{\text{vol}} [B]^T [D] [B] dv = \text{Element stiffness matrix}$$

$$\{F^{\text{th}}\} = \int_{\text{vol}} [B]^T [D] \{\epsilon^{\text{th}}\} dv = \text{Element thermal load vector}$$

$$\{\epsilon^{\text{th}}\} = \{\alpha\} \Delta T = \text{Thermal strain vector}$$

$$\{\alpha\} = \text{Vector of coefficients of thermal expansion}$$

In the current work, the effect of mechanical deformation on heat flow has been ignored and the thermo-mechanical phenomenon of melting is idealized as a sequentially coupled unidirectional problem. According to this simplified approach, a fully coupled thermal-metallurgical analysis is performed first which is followed by a structural analysis. During the thermal analysis, microstructure evolution can be modeled through either more sophisticated direct calculation procedure or by relatively simpler but common method of indirect incorporation of microstructure aspects into the material model. During the structure analysis, temperature and microstructure dependence of stresses and deformations are accommodated by invoking the results of thermal-metallurgical analysis into the stress analysis.

Table 2 Laser-assisted surface treatment conditions

Scanning speed, mm/min	Power, W	Peak power, W	Frequency, Hz	Nozzle gap, mm	Nozzle diameter, mm	Gaussian parameter, mm	Focus setting, mm	N ₂ pressure, kPa
100	160–180	2000	200	1.5	1.5	0.55	127	300

For thermal analysis, the given structure is modeled using thermal element (SOLID70). SOLID70 has a 3D thermal conduction capability. The element has eight nodes with a single degree of freedom, temperature, at each node. The element is applicable to a 3D, steady-state, or transient thermal analysis. Since the model containing the conducting solid element is also to be analyzed structurally, the element is replaced by an equivalent structural element (such as SOLID45) for the structural analysis. SOLID45 is used for the 3D modeling of solid structures. The element is defined by eight nodes having three degrees of freedom at each node; translations in the nodal *x*, *y*, and *z* directions. The element has plasticity, creep, swelling, stress stiffening, large deflection, and large strain capabilities.

2.2 Material Model

An accurate modeling of temperature-dependent material properties is a key parameter to the accuracy of computational mechanics and has been a challenging job due to scarcity of material data at elevated temperatures. In the computational mechanics, microstructure evolution is addressed either by direct calculations from thermal history, various phase fraction, properties of each constituent, and deformation history or indirectly by considering the micro-structural dependency on the thermal and mechanical history. Although the indirect approach is relatively crude it is widely used in the simulation due to its relative ease.

The thermal and structural properties used in the current simulations are given in Table 1(a) and (b). It should be noted that the conditions for the current simulations resemble the actual experiments carried out in the present study; the thickness of coating is 250 μm and thickness of the workpiece is 3 mm. Since the coating is melted by a laser beam during the simulations, no initial residual stress is considered due to the HVOF spraying process, i.e., during the melting, residual stress is relaxed in the coating.

3. Experimental

The CO₂ laser (LC-ALPHAIII), delivering nominal output power of 2 kW at pulse mode with different frequencies, is used to irradiate the workpiece surface. The nominal focal length of the focusing lens is 127 mm. Nitrogen assisting gas emerging from the conical nozzle and co-axially with the laser beam is used. The workpiece surface was scanned at a constant speed by a laser beam. Laser treatment conditions are given in Table 2. An aluminum substrate is used as the workpiece material.

JEOL JDX-3530 scanning electron microscope (SEM) and EDS are used to obtain photomicrographs of the cross section and surface of the workpieces after the tests. The Bruker D8 Advance having Mo-K α radiation is used for XRD analysis. A typical setting of XRD was 40 kV and 30 mA. It should be

noted that the residual stress measured using the XRD technique provides the data in the surface region of the specimens. This is because of the penetration depth of Mo-K α radiation into the coating, i.e., the penetration depth is in the order of 10-20 μm .

The residual stress measurement using the XRD technique relies on the stresses in fine-grained polycrystalline structure. The position of the diffraction peak undergoes shifting as the specimen is rotated by an angle ψ . The magnitude of the shift is related to the magnitude of the residual stress. Consequently, the precise measurement of this shift in a certain peak position in a diffraction pattern allows calculating the degree of strain within the coating. The relationship between the peak shift and the residual stress (σ) is given (Ref 11):

$$\sigma = \frac{E}{(1 + \nu) \sin^2 \psi} \frac{(d_n - d_o)}{d_o} \quad (\text{Eq 2})$$

where E is Young's modulus, ν is Poisson's ratio, ψ is the tilt angle, and d_i are the d -spacing measured at each tilt angle. If there are no shear strains present in the specimen, the d spacing changes linearly with $\sin^2\psi$. Figure 2 shows the d -spacing with $\sin^2\psi$. It can be observed that the variation is linear and no splitting occurs; therefore, the presence of shear strain is not notable. In addition, the slope is negative indicating that the stress is compressive.

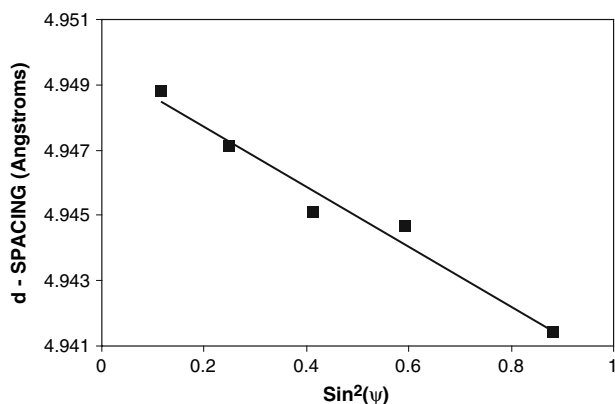


Fig. 2 d -spacing with $\sin^2\psi$ obtained from the XRD data

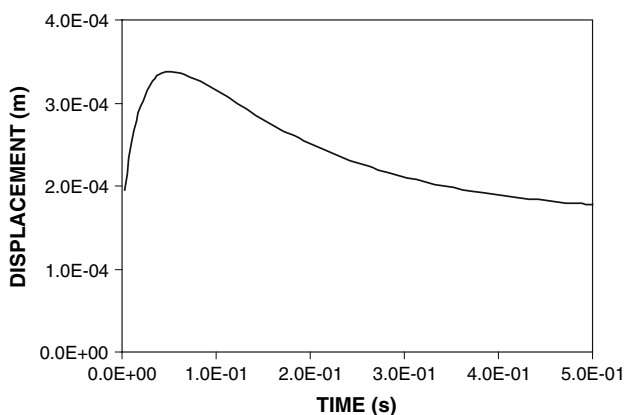


Fig. 3 Temporal variation of displacement at the mid-point of the specimen during the cooling cycle

4. Results and Discussions

Laser treatment of the HVOF coating is considered and the residual stress developed in the coating after the laser treatment process is examined. An experiment is carried out to melt the HVOF coating and the metallurgical changes in the coating after the laser treatment process are examined. The XRD technique is used to measure the residual stress in the coating.

Figure 3 shows the temporal variation of the displacement of the surface and along the y -axis as predicted from the simulation, while Fig. 4 shows dimensional view of the y -axis displacement. It should be noted that the cooling cycle is assumed to start at $t = 0$, i.e., initial heating phase (heating cycle) is not considered and at $t = 0$ coating is assumed to be at the melting temperature of the substrate material (Inconel 625). Moreover, temperature of the base material (Ti-6Al-4V) is kept at 460 K, which is lower than that of cooling at time $t = 0$. Although initially assumed that the displacement of the coating and the base material is zero at $t = 0$, because of the heat transfer from coating to the base material through the conduction as well as the heat transfer from coating to the surrounding environment by convection enable the base material and the coating to bend outward along the y -axis. This results in the displacement of the surface along the y -axis. Once the temperature gradient reaches a critical value, the surface displacement becomes maximum and prolonged cooling results in decreasing of the surface displacement. In this case, the temperature gradient reduces and the displacement along the y -axis reduces, accordingly. As the cooling period progresses further the displacement reduces gradually; however, it never reaches zero due to the residual stress developed in the coating during the cooling cycle. This situation is also seen from Fig. 4. This is because of the corresponding time, which is long enough for temperature to reduce to the room temperature, i.e., at the end of the cooling period.

Figure 5 shows temporal variation of von-Mises stress at three planes in the coating (reference to Fig. 1). von-Mises stress rises rapidly in the surface region (upper line) and remains the same with progressing time. The rapid rise of von-Mises stress is associated with the cooling rates in the surface region, which is high because of the convective heat

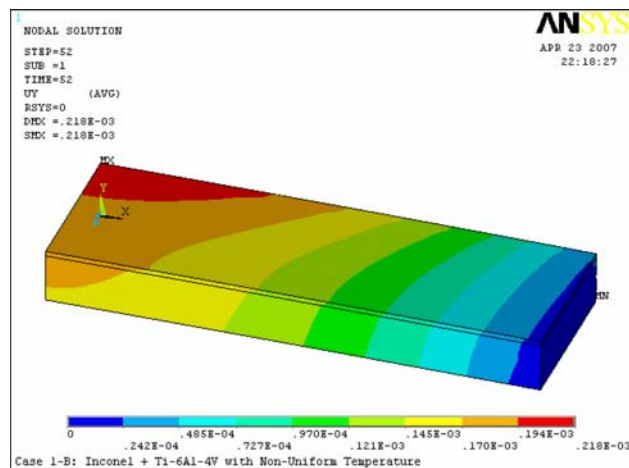


Fig. 4 3D view of displacement after ending the cooling cycle ($t = 0.5$ s)

transfer from the free surface to the surround ambient. However, as the time progresses further change in von-Mises stress is negligible and cannot be observed from the figure. In the case of the mid-plane, von-Mises stress attains almost the same value as that of in the surface region; von-Mises stress attains high values in the early heating period and decreases rapidly at the interface plane. This is because of the temperature gradient at the interface, which differs significantly from its counterpart in the surface region of the coating. The conduction heat transfer from the coating to the base material lowers temperature at the interface plane, since base material temperature is lower than that of the coating. As the time progresses, temperature of the base material increases at the interface plane because of the heat diffusion from the coating. This increases von-Mises stress with progressing time at the interface. During the cooling cycle, the cooling rate changes because of the

temperature gradient developed at the interface during the heating cycle. This modifies the residual stress levels once the cooling cycle is completed. It should be noted that for time period of 0.5 s, temperature of the coating reduces to about 530 K, which is considerably low and von-Mises stress after this time period can be considered as the residual stress in the coating and at the interface plane between the coating and the base material. Consequently, the residual stress at the coating-base material interface attains different values than that of in the coating. This can be observed from Fig. 5. Table 3 gives the

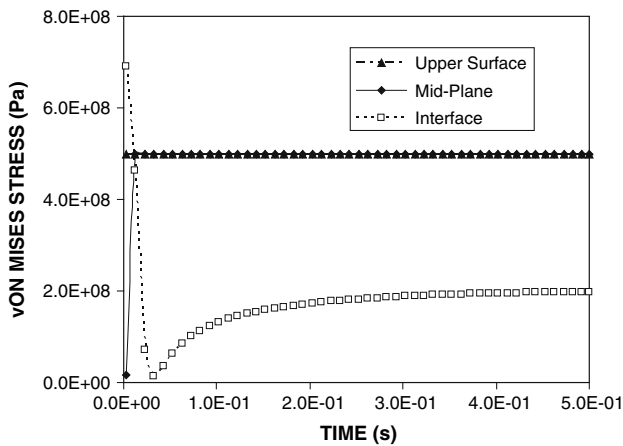


Fig. 5 Temporal variation of von-Mises stress at three planes (shown in Fig. 1) in the coating during the cooling cycle

Table 3 Residual stress predicted in the top plane and measured using the XRD technique

Residual stress predicted, MPa	Residual stress measured, MPa
350	330

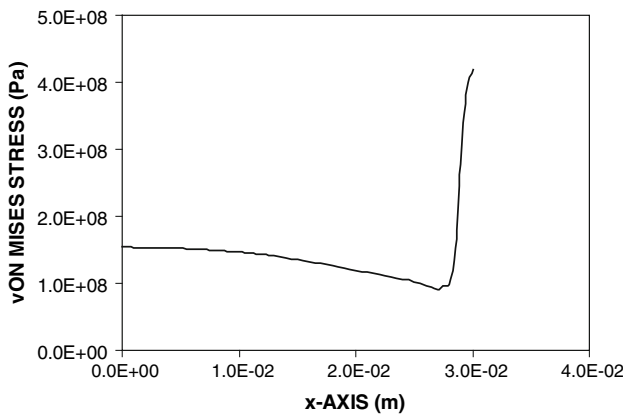


Fig. 6 von-Mises stress along the x-axis at the interface plane at the end of the cooling period ($t = 0.5$ s)

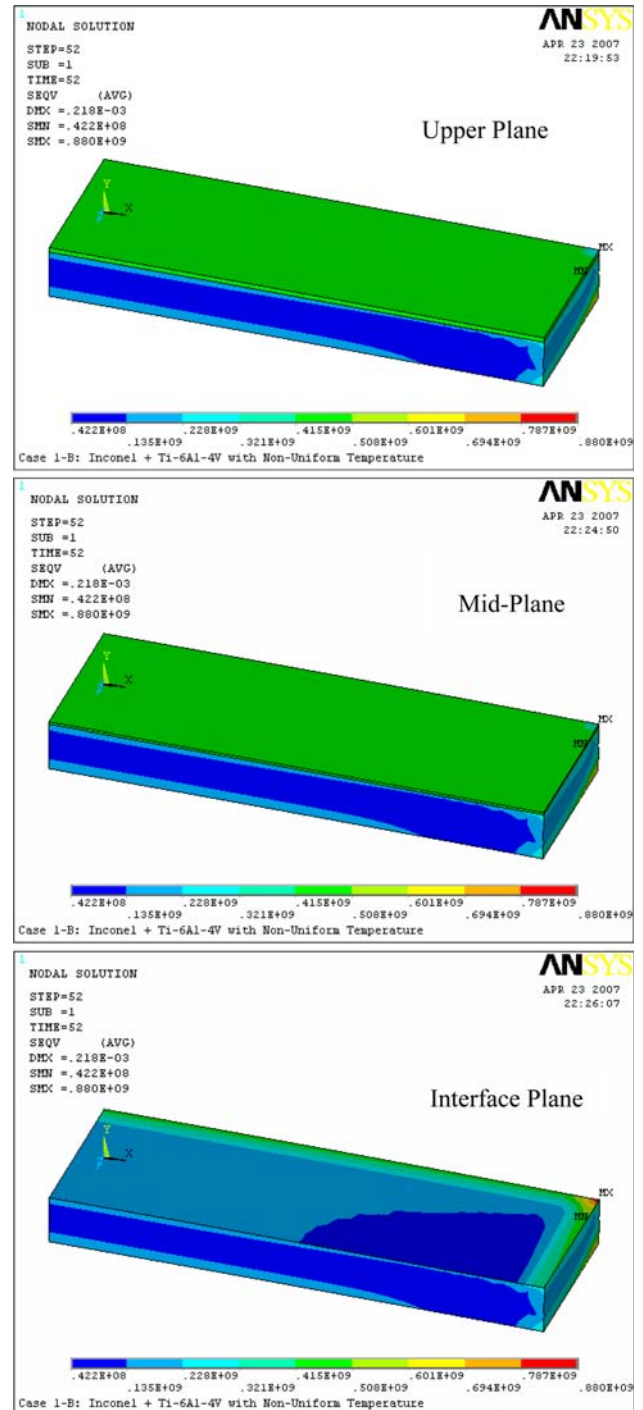


Fig. 7 von-Mises stress at three planes in the coating

residual stress predicted from FEM simulations and XRD measurements. It can be seen that von-Mises stress predicted agrees with the measurements result. It should be noted that von-Mises stress predicted in the top plane is given in the table for comparison. This is because of the fact that XRD measurement provides data with the 20 μm depth below the surface due to penetration limit of the Mo-K α radiation. However, when comparing von-Mises stress at different planes in the coating, it can be observed that von-Mises stress reaches minimum at the coating-base material interface; in other locations it remains almost the same.

Figure 6 shows von-Mises stress distribution along the axial direction (along the x -axis, Fig. 1) while Fig. (7) shows von-Mises stress distribution in the coating and the base material. von-Mises stress in the center of the specimen at the mid-plane is in the order of 150 MPa and as the distance increases toward the edge of the specimen, it reduces gradually, provided that it increases sharply in the region at the specimen end. This increase is associated with the fixed end of the specimen. In the analysis, to resemble the actual spraying situation, both ends of the specimen are fixed similar to the case in the experiments.

Figure 8 shows the top and cross-sectional view of HVOF-coated samples prior and after the laser treatment. The top view of the coating reveals that some of the splats de-bond in the surface region where the oxygen concentration is high (Table 4, in which EDS analysis is given). The de-bonding is mainly through the oxide interfaces. In addition, some small, elongated splats are also observed. Despite the fact that the oxide particles promote high stress concentration in the surface region, no crack is evident in the surface region. In case of HVOF coating cross section, lamellar structure and locally and randomly

distributed voids in between the splats are observed. In the coating, the regions around the splats boundary reveal the existence of the oxidation during in-flight before impacting the coating surface. Moreover, some stringers like inclusions are also evident in the coating. These are highly oxide particles in the coating. In the case of the laser-treated specimens, the complete melting of the coating is evident from the micrographs. In addition, the micro-holes, formed due to the gasification and the bubbles formed during the melting, is not evident in the melt region. This is mainly because of the low scanning speed of the laser beam; consequently, bubbles formed during the laser melting coalesces and escape during the melting and voids formed by the bubbles are filled with the liquid metal due to the surface tension force. The oxide formed around the splats partially disappears due to the melting and mixing in the coating. This situation is particularly seen from the SEM micrograph (Fig. 8). Moreover, the laser-melted region is compact and sealing effect of the melt layer at the coating surface is evident, i.e., the spreading or partially melted splats at the surface are not observed. Although the cooling rate at the surface is high, upon solidification no micro-crack is observed from the micrographs. During the laser melting of coating, the residual stress developed in the coating during the

Table 4 EDS results after the laser treatment process

Location below surface	O	Al	Cr	Fe	Ni
5 μm	11.87	0.21	16.98	Balance	30.28
20 μm	7.23	0.32	16.18	Balance	31.60

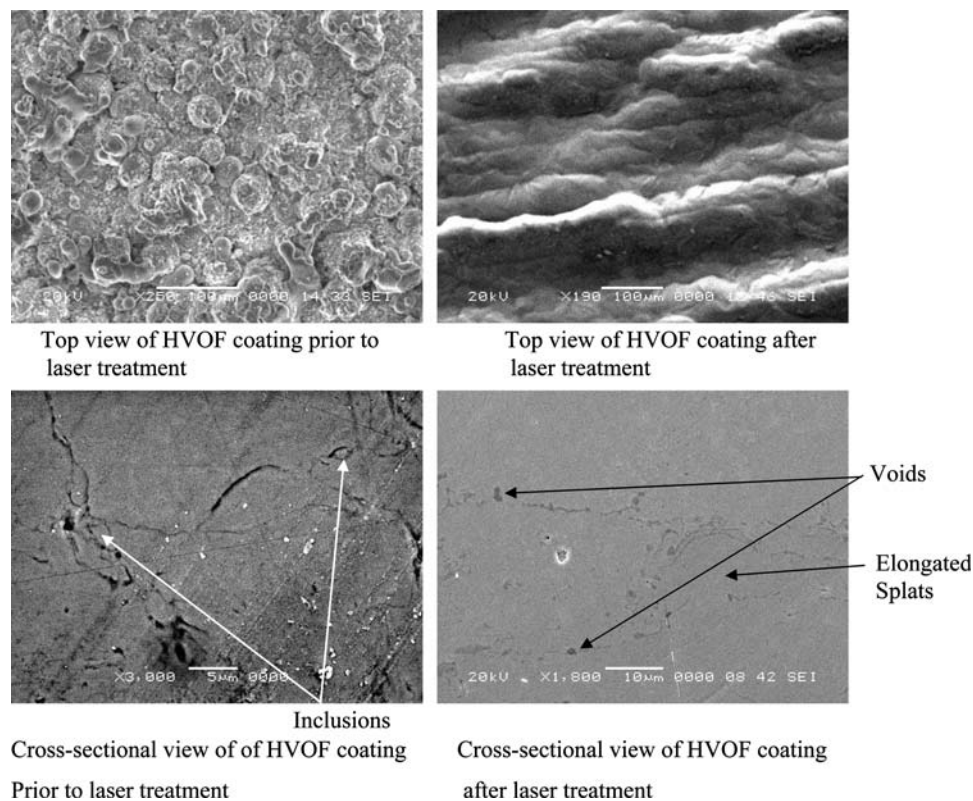


Fig. 8 SEM micrographs of as-received HVOF coating and laser-treated coatings

HVOF spraying process is relaxed. However, changes in the cooling rate as well as the effects of high cooling rate on the solidification process in the coating during the cooling cycle result in the residual stress development in the coating as well as at the coating-base material interface.

5. Conclusion

Laser treatment of HVOF of coating is considered and the residual stress field in the coating is modeled using the finite element method. The time duration in the cooling cycle is extended such that temperature in the coating reduces to almost room temperature. In this case, the stress field predicted in the coating represents the residual stress formed after the laser treatment process. An experiment is carried out to examine the morphological and metallurgical changes in the laser-melted layer. It has been found that the residual stress predicted in the surface region is in the order of 350 MPa and it reduces to 150 MPa at coating-base material interface. The attainment of low residual stress at the interface plane is associated with the heat diffusion from the coating to the base material, which modifies the temperature gradient in this region. Consequently, temperature gradients in the coating and across the interface plane differ significantly. This agrees well with the XRD measurements of the residual stress. The surface displacement predicted remains positive, which agrees with the experimental observations. This indicates that the residual stress field is compressive. The melting modifies the coating structure, in which case, a compact coating with excellent sealing at the surface is observed. Although the cooling rates are high at the surface due to convective boundary, no cracks or spreading of splats are observed. In addition, oxide formation around the splat boundary almost disappears due to the melting and mixing in the coating. The voids in the coating disappears and the bubble sites formed during the melting, due to initial capture of air in HVOF coating process, is replaced with the molten metal through the surface effect. This lowers the porosity during the melting and solidification process.

Acknowledgment

The authors acknowledge the support of King Fahd University of Petroleum and Minerals Dhahran Saudi Arabia.

References

1. J. Tuominen, P. Vuoristo, T. Mantyla, M. Kylmalahti, J. Vihinen, and P.H. Anderson, Properties of Nickel Superalloy Coatings As-Sprayed and with Nd-YAG Laser Remelting, *Proceedings of the International Theme Spray Conference*, 2000, p 589–596
2. H. Hamatani and Y. Miyazaki, Optimization of an Electron Beam Remelting of HVOF Sprayed Alloys and Carbides, *Surf. Coat. Technol.*, 2002, **154**, p 176–181
3. M. Oksa, E. Turunen, and T. Varis, Sealing of Thermally Sprayed Coatings, *Surf. Eng.*, 2004, **20**(4), p 251–254
4. J. Suutala, J. Tuominen, and P. Vuoriso, Laser-Assisted Spraying and Laser Treatment of Thermally Sprayed Coatings, *Surf. Coat. Technol.*, 2006, **201**, p 1981–1987
5. A. Hjornhede and A. Nylund, Adhesion Testing of Thermally Sprayed and Laser Deposited Coatings, *Surf. Coat. Technol.*, 2004, **184**, p 208–218
6. S. Kumari, A.S. Khanna, and A. Gasser, The Influence of Laser Glazing on Morphology, Composition and Microhardness of Thermal Sprayed Ni-WC Coatings, *4th International Surface Engineering Conference*, Aug 1-3, 2005, St. Paul, MN, USA
7. M. Riabkina-Fishman, E. Rabkin, P. Levin, N. Frage, M.P. Dariel, A. Weisheit, R. Galun, and B.L. Mordike, Laser Produced Functionally Graded Tungsten Carbide Coatings on M2 High-Speed Tool Steel, *Mater. Sci. Eng.*, 2001, **A302**, p 106–114
8. J. Tuominen, P. Vuoristo, T. Mantyla, M. Kyimalahti, J. Vihinen, and P.H. Andersson, Improving Corrosion Properties of High-Velocity Oxy-Fuel Sprayed Inconel 625 by Using a High-Power Continuous Wave Neodymium-Doped Yttrium Aluminum Garnet Laser, *J. Therm. Spray Technol.*, 2000, **9**(4), p 513,
9. B.S. Yilbas, A.F.M. Arif, and M.A. Gondal, HVOF Coating and Laser Treatment : Three-Point Bending Tests, *J. Mater. Process. Technol.*, 2005, **164–165**, p 954–957
10. B.S. Yilbas, M. Sami, and H.I. Abu Al-Hamayel, 3-dimensional modelling of laser repetitive pulse heating: a phase change and a moving heat source considerations, *Appl. Surf. Sci.*, 1998, **134**, p 159–178
11. T.C. Totemeier, R.N. Wright, and W.D. Swank, Residual Stresses in High-Velocity Oxy-Fuel Metallic Coatings, *Metall. Mater. Trans. A: Phys. Metall. Mater. Sci.*, 2004, **35**(6), p 1807–1814